Russian Geology and Geophysics
Vol. 43, No. 4, pp. 343-363, 2002

Geologiya i Geofizika
UDC 551.22+552.11

PYROXENITE XENOLITHS IN PICRITE BASALTS (*Vitim Plateau*): ORIGIN AND DIFFERENTIATION OF MANTLE MELTS

I.V. Ashchepkov and L. André*

United Institute of Geology, Geophysics and Mineralogy, Siberian Branch of the RAS, 3 prosp. Akad. Koptyuga, Novosibirsk, 630090, Russia
** Musée Royal de l'Afrique Centrale, Département de Géologie, Leuvensesteenweg 13, Tervuren, 3080, Belgium*

The petrography and major- and trace-element chemistry of pyroxenite xenoliths from Miocene picrite basalts of the Vitim plateau suggest an origin by polybaric fractional crystallization of mantle melts. High-temperature giant-grained black pyroxenites and clinopyroxene megacrysts make a long trend (Fe# = 0.12 to 0.23%) corresponding to polybaric Cpx-Ga cotectic fractionation, possibly, associated with formation of a pre-eruption vein system. Low-temperature black pyroxenites are products of interaction of residual melts with the lower crust material. High-temperature hybrid websterites may have been produced by mixing of basaltic melts with fused (<5–10% partial melting) metasomatic mantle lherzolites or by AFC processes with Ga-Cpx dissolution. Anatectic Cr pyroxenites were formed mostly by segregation of partial melts from lherzolite material and remelting of former veins. Low-temperature hybrid garnet pyroxenites result from interaction of metasomatic lherzolites (or earlier Cr-diopside veins) with volatile-enriched differentiated basaltic melt. Remelting of earlier mineral generations, which occurs in all rising melt systems, is reflected by mirror-like peaks on spidergrams, spikes on TRE diagrams, and LREE and HFSE (and ore element) enrichment.

Megacryst, basalt, clinopyroxene, garnet, ilmenite, mantle, melt, fractional crystallization, partition coefficients, melting, assimilation, inductively coupled plasma

INTRODUCTION

Implications for differentiation of mantle melts are usually based on compositional variations in erupted volcanic suites [1, 2] or layered intrusions [3]. However, magma differentiation within the spinel and garnet facies can be inferred only using reliable thermobarometry and partition coefficients applied to pyroxenite mantle xenoliths and megacrysts [4, 5]. Our study is based on a large collection of pyroxenite mantle xenoliths from Miocene picrite basalts of the Vitim plateau [6] which include several suites distinguished by continuous compositional trends, petrography, and chemistry. The model compositions of their parent melts [7] correspond to several magma types: (a) produced by partial melting of lherzolite mantle; (b) OIB-type continental alkali basaltic melts derived from mantle plumes; (c) melts with spectra typical of continental-margin andesite basalts or lower crust anatectic melts; (d) hybrid varieties. Compositional variations in vein cumulates (with observed or hypothesized contact relationships) are most often caused by interaction of basaltic magmas with mantle peridotites or crustal substrate and related hybridization.

Megacrysts are usually interpreted as deep-seated precipitates from basaltic melts, and their compositions are used to calculate partition coefficients (e.g. in [5, 8]). This is not strictly correct, as less radiogenic $^{87}Sr/^{86}Sr$ ratios [9, 10] and steeper REE plots of their parent melts [11] are inconsistent with complete phase equilibrium with the host lavas. Some megacrystalline varieties of Vitim xenoliths rarely coexist with other pyroxenites or dunites within a sample and are apparently mantle pegmatitic veins. The origin of pyroxenite and amphibole-phlogopite vein suites of mantle xenoliths has caused much discussion [12, 13]. The diversity of the Vitim pyroxenite xenoliths

and relationships of their varieties provide a good basis for realistic genetic interpretation, and precise analytical data enable numerical modeling of evolution and interaction of melts with the host peridotites.

METHODS

Mineral grains of pyroxenite and peridotite nodules mounted in epoxy were analyzed on a Camebax-Micro X-ray microprobe at the United Institute of Geology, Geophysics and Mineralogy, Novosibirsk (operator O. Khmel'nikova), at 20 keV and 100 mA. Samples 315-(1-100), 250-257, 320-(1-24), 327-(1-9), and some samples from the 315-(400-695) series were analyzed by I. Ashchepkov; samples 315-(100-181) were analyzed by Yu. Litasov, 315-(200-313) by S. Strizhov, 315-340, 315-342 and some others by K. Litasov. Samples 315-(136, 222, 325, 326, 414, 440) were analyzed by I. Ashchepkov in thin sections on a Cameca-50SX microprobe in the Catholic University of Leuven (Belgium).

Analytical procedure for trace elements. REE and other trace elements in monominerals (several samples of each group of pyroxenites in the collection) were analyzed by ICP-MS on a VG elemental Plasmoquad (PQ 2 Turbo Plus) at the Royal Museum for Central Africa (Tervuren, Belgium) by L. André, J. Naves, with participation of I. Ashchepkov.

Carefully hand-picked separates of pyroxene, garnet, and other minerals were leached first in 15% HCl for 15 minutes, then in 5% HF, and then in concentrated HF, with untrasound-assisted rinsing in distilled water after each step. The leached minerals were completely digested a mixture of three Suprapur Merck acids (HF : 4; HNO_3 : 1; $HClO_4$: 1) in high-pressure Teflon vessels at 180 °C. After removal from the vessels, the solution was diluted in $HClO_4$ and dried. The remaining solid was redissolved in HNO_3. The solution was placed in 50 ml volumetric flasks and made to volume with 5% HNO_3 containing reference quantities of four internal tracers (Ru, Bi, Re, In).

For details of the ICP-MS procedure see [14]. The ionized sample was introduced into the chilled spray chamber of the instrument operated at 0.75 l/min Ar flow rate. The ICP-MS was optimized with a 10 ppb solution of ^{115}In and ^{238}U to gain a typical sensitivity of $5 \cdot 10^4$ counts $\cdot$ $sec^{-1} \cdot ppb^{-1}$ on ^{115}In. Each sample was measured in triplicate with a reagent blank and interference corrections running five natural (PCC-1, DTS-1, AN-G, W1, BHVO-1) and four artificial international standards. Analytical precision was < 5% for REE, 10–15% for HFSE and somewhat higher for LILE; the reproducibility ranged between 0.2% for REE and 3% for LILE.

PETROGRAPHY

Low-Cr green megacrystalline clinopyroxenites occur as large (5–10 cm) crystals or aggregates often with rounded orthopyroxene inclusions (up to 5%) and numerous gaseous blebs (*1* in Fig. 1); some are giant-grained websterites containing equal proportions of pyroxenes, with curvilinear contacts.

Dark-green websterites consist of 2–5 cm round crystals (*2* in Fig. 1). Smaller orthopyroxene grains appear inside clinopyroxene crystals or in intergranular space. Some larger xenoliths show graded layering.

Black (dark-brown) garnet pyroxenites are most often aggregates of 3–7 cm grains with round or curvilinear boundaries. Some black clinopyroxenites form druse-like aggregates of 0.5–2 cm crystals similar to those found on Shavaryn-Zaram volcano [15]. In sample 315-421 they are crushed and cemented with gaseous and fluid-saturated aggregate of later augite crystals (*3* in Fig. 1). Garnet occurs either in outer zones of augite crystals or in intergranular space where it coexists with small (few millimeters) orthopyroxene grains. In few garnet-rich samples it cements strained (twisted) clinopyroxene grains (*4* in Fig. 1). Darker varieties often appear as single crystals with fragments of flat free growth surfaces of natural augite with dissolution-growth sculptures on them. Giant-grained black monocrystalline blocks (up to 40 cm) are often partly substituted by brownish aggregates with magnetite globules in light pyroxene; the aggregates may be fused and contain new pyroxene, plagioclase, or spinel. Some pyroxenes of this type include chains of gas cavities enclosing up to 3 mm drop-like ilmenite and Ti-biotite grains [16] (*7* in Fig. 1); however, normally ilmenite makes platy inclusions scattered in black pyroxenes. Disseminated sulfides occur in all black pyroxenites and interstitials and often appear (occasionally up to ~1%) in outer zones of garnet.

Plagioclase websterites are either gneissic plagioclase-bearing websterites with garnet usually inside clinopyroxene grains (*5* in Fig. 1) or with amphibole (occasionally clinopyroxene-phlogopite-amphibole) intergrowths, or are essentially clinopyroxenite coarser-grained varieties of a cumulate structure with interstitial plagioclase and orthopyroxene.

Gray garnet clinopyroxenites (to garnetites) with partially kelyphitic garnet vary in structure, size, and grain

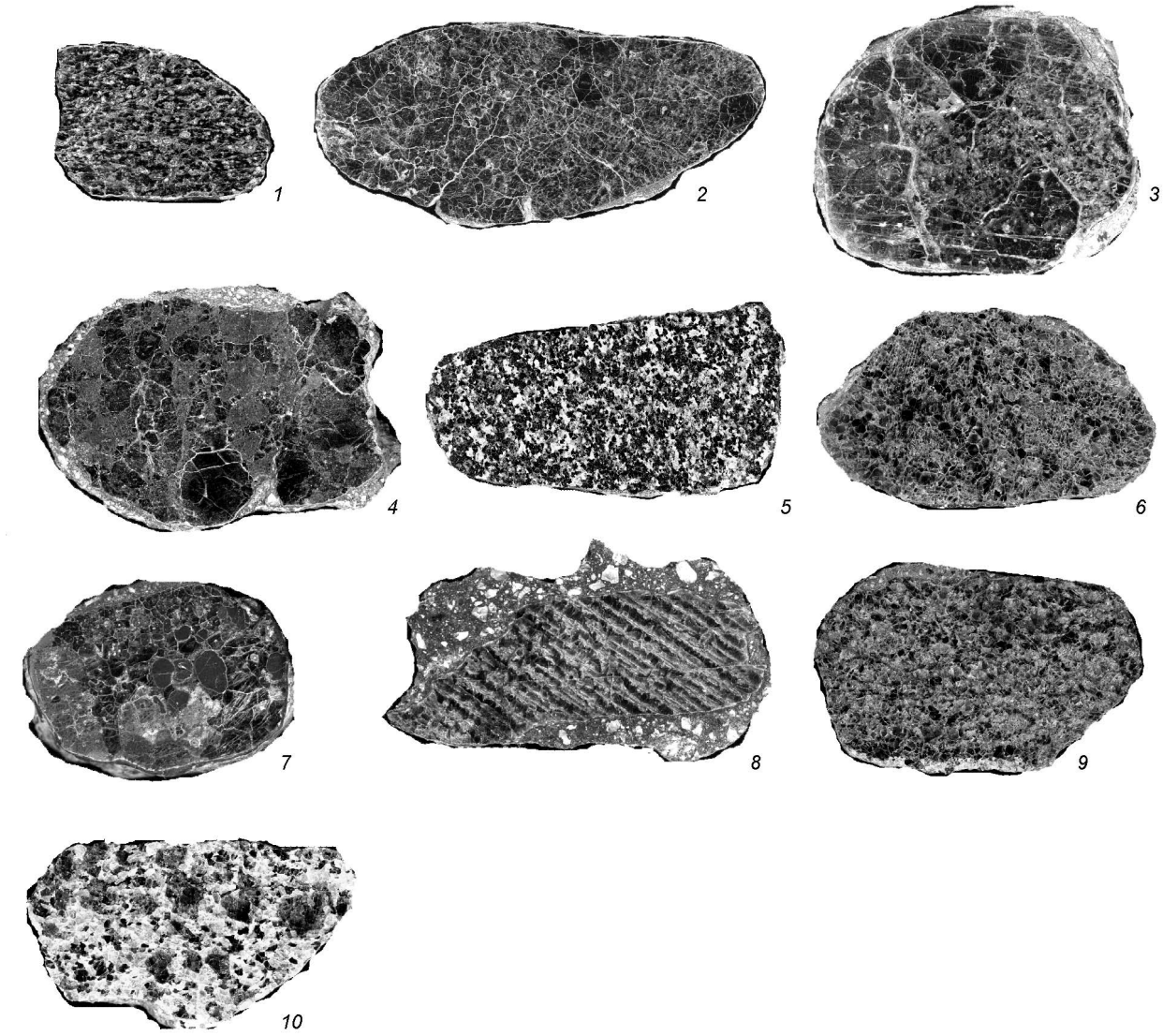

Fig. 1. SEM images of pyroxenites. *1* — HT green clinopyroxenite with ingrown orthopyroxene and numerous fluid-filled cavities; *2* — HT green websterite; *3* — druses of black pyroxene crystals filled with later pyroxene aggregate; *4* — black garnet pyroxenite; *5* — gneissic pyroxene-plagioclase cumulate; *6* — Cr-Di garnet websterite with garnet lamellae in clinopyroxene; *7* — gray-green garnet clinopyroxenite with round ilmenite inclusions; *8* — Cr-Di clinopyroxenite with notched orthopyroxene lamellae; *9* — contact of Cr-Di garnet pyroxenite with lherzolite; *10* — lherzolite with ingrown coarse garnet grains cut with phlogopite.

morphology. Structures vary from poikilitic with garnet intergrown into clinopyroxene to coarse pegmatitic crystals. One garnet websterite sample of this type was found in contact with lherzolite.

Green Cr-Di pyroxenites of diverse structures and chemistry [17] often show curvilinear contacts with the host lherzolites (*10* in Fig. 1) or occasionally distinct signs of intrusion with sharp contacts (*9* in Fig. 1). Asymmetrical inner structure of the xenoliths is often made by different grain sizes of garnet and clinopyroxene or less often by spinel and their aggregates (*9* in Figs. 1). Some large Cr-Di crystals contain elongate and notched or thin plane-parallel garnet or orthopyroxene lamellae similar to pegmatitic ichtyoglyphs (not to be confused with exsolution lamellae) (*8* in Fig. 1).

MAJOR-ELEMENT VARIATIONS IN CLINOPYROXENES AND GROUPING OF MANTLE XENOLITHS

The chemical systematics of pyroxenites is based on major element variations in clinopyroxene, the through phase in the studied mineral associations. The high Mg# (low-Fe#) domain comprises two fields of **high temperature (HT) giant-grained green websterites** (Fig. 2) with different Cr contents rapidly decreasing with increasing Fe# (Fe# as Fe/(Fe + Mg) a.u.). TiO_2, Na_2O, and Al_2O_3 show strong variations at similar FeO contents. The clinopyroxenes of this type plot steep FeO–CaO trends (Fig. 3) corresponding to a temperature range of 1350 to 1200 °C. Variation diagrams for **black megacrysts and giant-grained pyroxenites** (*1*, *2* in Fig. 2) reveal positive correlation of Fe with Ti, Al, Na, and Ca starting with dark green websterites (*1*, *2* in Fig. 2), usually

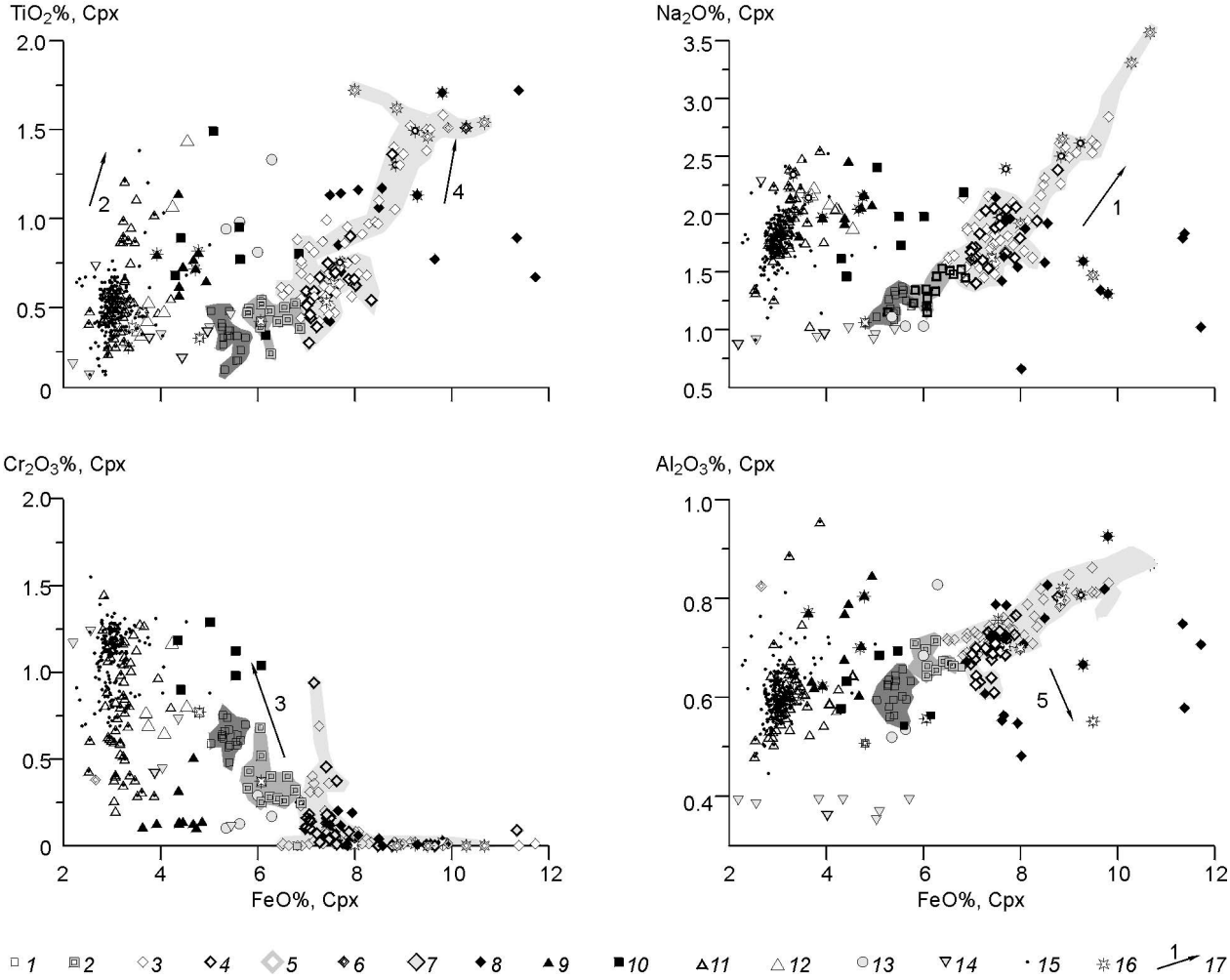

Fig. 2. Variation diagrams for clinopyroxenites from deep-seated pyroxenite xenoliths in picrite basalts. *1* — HT green clinopyroxenites (websterites); *2* — HT dark-green green hybrid pyroxenites; *3* — black megacrysts and giant-grained pyroxenites; *4* — same with garnet; *5* — same without visible garnet with ilmenite and Ti biotite; *6* — pegmatitic high-Na clinopyroxenites with numerous cavities; *7* — high-Fe# plagioclase-bearing pyroxenites; *8* — shallow cumulates with plagioclase; *9* — MT hybrid gray garnet pyroxenites; *10* — veins with kaersutite, phlogopite, and pyroxenite rims; *11* — anatectic Cr-Di pyroxenites; *12* — high-Fe# Cr-Di veins; *13* — LT hybrid veins; *14* — low-Al veins; *15* — lherzolites; *16* — samples analyzed for REE by ICP-MS; *17* — trends of pyroxene compositions associated with fractionation of clinopyroxene (and garnet) (1), differentiation of Cr-Di veins and remelting of earlier metasomatites (2), assimilation of peridotites (3), dissolution and precipitation of ilmenite (4), and precipitation of plagioclase (5).

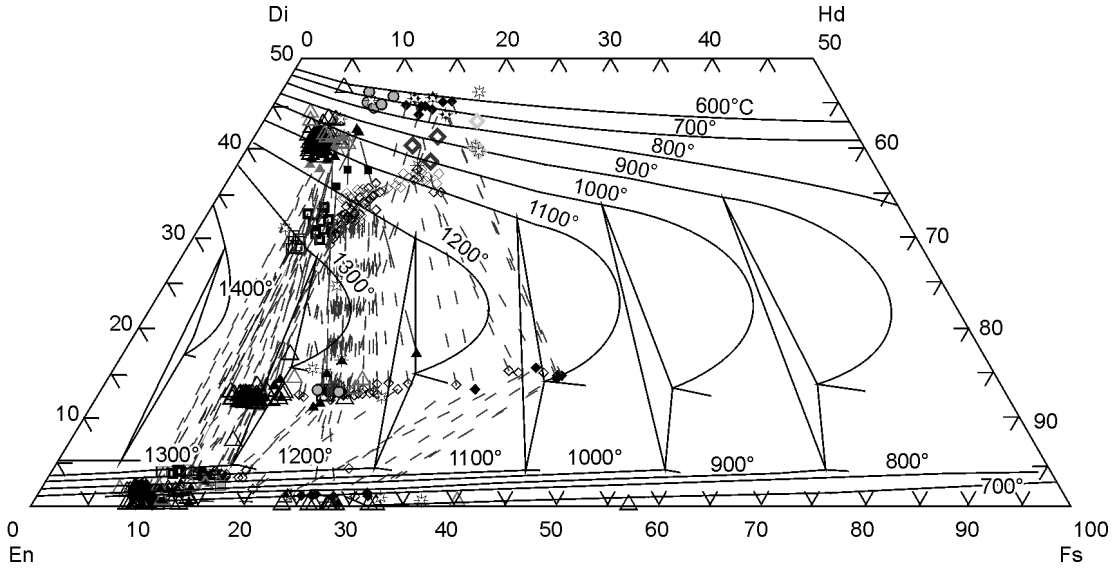

Fig. 3. En-Di-Hd-Fs diagram with solidus lines for pyroxenes after [14] and compositions of mineral pairs: clino- and orthopyroxenes, garnets from pyroxenite mantle xenoliths in Vitim picrite basalts. For legend see Fig. 2.

related to fractionation. At a closer look this trend consists of differently sloping segments, some even perpendicular to the main trend (Fig. 2) likely due to precipitation of new phases and assimilation of wall peridotites. The co-ascending trend starts with garnet-bearing pyroxenites and ends with giant-grained (up to 40 cm) clinopyroxene crystals (*5* in Fig. 2). The ilmenite- and phlogopite-bearing aggregates are slightly earlier precipitates [16] (*10* in Fig. 2), like the Malaita megacrysts from the Solomon Islands [17]. Clinopyroxenes of **plagioclase websterite** cumulates (*7*, *8* in Fig. 2) either fall near the megacryst trend or are lower in Fe#, Ti, Al, and Na because of crystallization of plagioclase and ore minerals.

Low Cr (0.1–0.4%) **hybrid gray garnet clinopyroxenites** (*9* in Fig. 2) plot a separate field (with Fe# intermediate between Cr-Di and megapyroxenite suites) which splits into two Al subtrends. Clinopyroxenes in them are relatively high in Na, Al, and Ti. Clinopyroxenes surrounding **kaersutite-phlogopite veins** (*10* in Fig. 2) in garnet and spinel lherzolites continue the high-agreement Fe# segment of the trend along with some anhydrous Fe-Cr diopside websterites.

Cr-Di pyroxenites are of two groups (*11*, *12* in Fig. 2) that represent (i) a magmatic trend of jointly ascending Fe, Na, Ti, Al, and Ca in clinopyroxenes, which falls outside the field of lherzolites and (ii) a subsolidus trend of decreasing Fe and increasing Ca (Fig. 3) typical of lherzolites from many localities. The FeO–Cr_2O_3 variation diagram shows a fractionation trend of decreasing Cr_2O_3 near the lherzolite field, a megacryst and an intermediate trends. The mineral chemistry of garnet lherzolites is generally similar to that of Cr-Di pyroxenites except for higher Cr and slightly lower Na, Ti, and Al [18].

THERMOBAROMETRY

Crystallization temperatures (Fig. 3) were estimated using the pyroxene quadrilateral with the 15 kbar solvus calibration according to Lindsley [19] and two-pyroxene geothermometers of Bertrand-Mercier [20] and Brey-Köhler [21] (Fig. 4). Pressures were estimated following Brey-Köhler and Nickel-Green equations [21, 22]. As a result, we modeled the *PT* history of pyroxenites in spite of some disagreement of *PT* estimates from different mineral pairs. The two-pyroxene [19] (*T*, °C) and Ga-Opx [22] (*P*, kbar) pairs (Fig. 4, *a*) suggest the black garnet megaclinopyroxenites with interstitial orthopyroxene to be the deepest xenoliths with their *PT* estimates close to the values of partially molten sheared peridotites [23]. They follow a high-temperature (but colder than basaltic) subadiabatic *PT* branch in a range of 32 to 25 kbar, then, discontinuously, to 14 kbar (with already slightly contaminated Cr varieties), and finally to the lower-crust pressures. Finer-grained black garnet clinopyroxenites, occasionally with hydrous minerals, form a small cluster around 20 and 14–16 kbar in the low-temperature region (Fig. 4, *a*), intermediate between the lherzolite and megapyroxenite *PT* fields. The plots of black plagioclase cumulates correspond to lower-crust or Moho conditions; the *PT* field of Cr-Di pyroxenites is similar to the

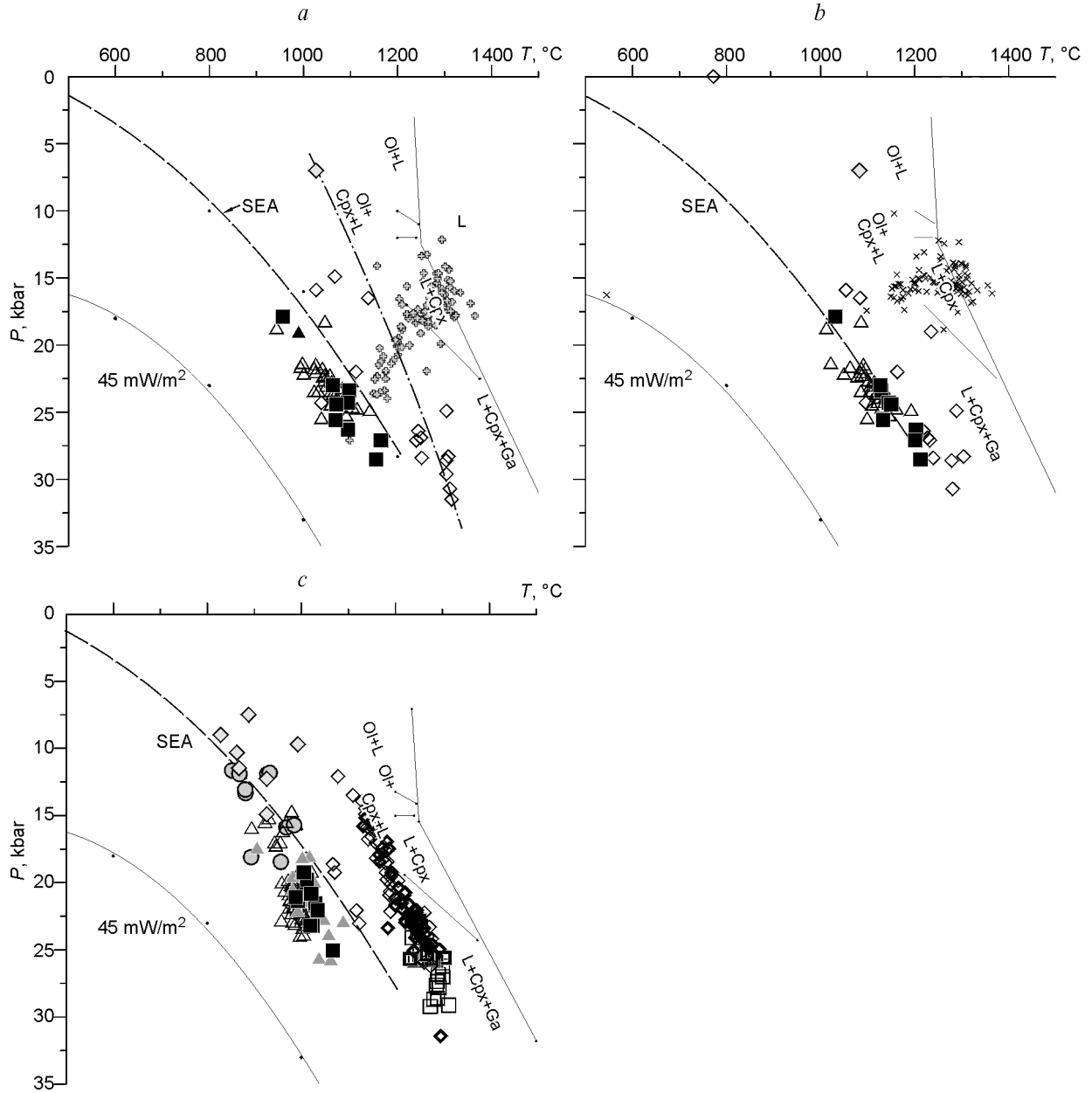

Fig. 4. Thermobarometry of pyroxenite xenoliths, from different methods. *a*: Bertrand-Mercier geothermometer [20], Nickel-Green geobarometer [22]; *b* — Brey-Köhler thermobarometry [21]; *c* — corrected (see text) Mercier clinopyroxene thermobarometry [24]. Additionally shown are *PT* conditions for black pyroxenes with pressure estimates after [26] (pluses, in *a*) and [27] (crosses, in *b*). Temperatures were estimated after [24] (see text). Liquidus and hyper-solidus lines for basanite are after [31]. For legend see Fig. 2.

lherzolite field but shows a slightly higher temperature (highest temperatures were obtained for high-Fe# varieties). Another field in the mid-temperature domain corresponds to Cr websterites with low-Al clinopyroxenes, of which one sample contained graphite [Litasov, pers. commun.]. The Brey-Köhler geothermobarometry [21] gives similar *PT* estimates but slightly shifted towards higher temperatures and lower pressures (Fig. 4, *b*).

The Mercier thermobarometry [24] shows an almost continuous *PT* trend for high-temperature megapyroxenites (Fig. 4, *c*). The greatest depths inferred for green garnet-free varieties appear plausible as liquidus temperatures of garnet in picrites correspond to much higher pressures [25]. Other pressure intervals nearly coincide. The high-temperature trend consists of several segments with slightly different *PT* gradients, apparently,

corresponding to different batches of magma in the vein system (cf. *a*, *b*, *c* in Fig. 4). Black pyroxenites also show at least three temperature trends (Fig. 3, near the Di corner). Gray garnet pyroxenites make a *PT* cloud between black megapyroxenites and Cr-Di websterites with higher-temperature Fe-rich varieties.

The Nimis liquidus barometry [26, 27], in which pyroxene chemistry is used to estimate cell volume, gives a better constrained crystallization interval of megacrysts (Fig. 4, *a*, *b*; techniques applicable to subalkalic compositions). Combined with Bertran-Mercier thermometry, this method gave no regular geotherm and even inverse gradients (Fig. 4, *a*), but the pressure range of 12 to 25 kbar agrees well with the common Opx-Ga barometry.

The lower pressure limit of ~20 kbar, estimated from equations for anhydrous alkali basalt melts [25] approaches the pressure estimates for garnet lherzolites in the Vitim plateau [28, 29]. However, our results [7, 16, 23, 30] indicate deeper magma generation, fractionation, and trapping of xenoliths.

Assuming liquidus crystallization of clinopyroxenes from megacrystalline pyroxenites and further subliquidus fractionation of garnet and other phases, the temperature of ~1400 °C can be interpreted as corresponding to at least 27 kbar, according to the known liquidus for alkali melts [31]. However, any version of geothermobarometry implies rather subliquidus cotectic crystallization of megapyroxenites in which the precipitates could reach complete equilibrium with the melt. Variations of pyroxenes in some garnet peridotites (e.g. sample 315-222) cover a half of the garnet pyroxenite range (Fig. 4), and the obtained *PT* estimates also show scattered temperatures and pressures of 2–3 kbar.

Polybaric fractionation is inferred from most of existing barometers, especially structural ones [26, 27], possibly, because of their strong temperature dependence. Yet, the polybaric conditions are confirmed by phase relationships at the alkali-basalt subliquidus, namely the succession of intergranular minerals from garnet and orthopyroxene to ilmenite and shallower plagioclase (and biotite).

Al^{VI}/Al^{IV} ratios for megapyroxenites (Fig. 5), as another independent proof for polybaric fractionation [32], agree with the pressure decline. Both Al^{VI} and Al^{IV} increase with Fe#, Al^{VI} showing, however, several slightly different trends. Even varying within each group of pyroxenites, the Al^{VI}/Al^{IV} ratios plot a generally descending trend (Fig. 5), especially for black megapyroxenites and shallow cumulates. This suggests uniform vertical distribution of megapyroxenites and Cr-Di pyroxenites, though the former are slightly deeper and HT green websterites contain less Al^{VI}.

TRACE ELEMENT CHEMISTRY IN DIFFERENT GROUPS OF XENOLITHS

The major and trace element chemistry of minerals in pyroxenite xenoliths of Vitim picrite basalts and implications for behavior of trace elements are given in more detail in [6]. Major oxides, F, and Cl were analyzed by EMPA and trace elements by ICP-MS (Table 1).

Black giant-grained pyroxenites show a gradual increase in LREE and MREE abundances with Fe# (by fractionation of clinopyroxene) and a decrease in HREE (by precipitation of garnet) (Fig. 6, *b*, *c*). **HT black garnet pyroxenites** (Fig. 6, *d*) have lower Sm/La_n and Gd/Yb_n ratios in the flatter middle part of the REE plot. Rb, Ba, Th, U, and Nb contents are variable. These patterns are typical of high-temperature basaltic melts [33, 34], though the calculated HFSE (Nb, Ta, Zr, Ti, Y) partition coefficients for garnets approach the experimental values for carbonatites [35, 36], possibly because of high CO_2 content.

HT green websterites (Fig. 6, *e*), compositionally similar to black megapyroxenites, show lower REE abundances and La/Yb_n ratios and higher LILE and HFSE contents. Higher-Fe# pyroxenes of this group have Rb-Nb spectra as in the black suite, and others are closer to green Cr-Di veins with elevated Nb, U, and Ba.

Shallow black plagioclase clinopyroxenites and websterites (Fig. 6, *a*) show LREE maxima and deep Ta-Nb, Pb, and Sr minimums typical of melts and cumulates fractionated in strongly oxidizing conditions at relatively shallow depths. Clinopyroxenes in plagioclase websterites have high total REE contents with variable La/Sm_n and Gd/Yb_n ratios and elevated Th and U relatively to peridotites.

The REE patterns of **mid-temperature (MT) hybrid gray pyroxenites** (Fig. 7, *b*) are the most exotic, similar to those of phlogopites [37], occasionally two-folded, with mirror-like patterns of LREE (Cs, Rb, Ba, and U) and symmetrical Sm-Nd peaks and Pb-Zr dips. The patterns of pyroxenes from amphibole-phlogopite veins radiate fan-like in the HREE part (Fig. 7, *a*).

Cr-Di veins have diverse trace-element patterns (Fig. 7, *c*) and split into two main groups: (i) with stronger Ta and Nb and weaker U and Th enrichments, and (ii) with mirror-image dips of these elements. Clinopyroxenes in Cr-Di veins show variable slopes of (La/Sm_n and Gd/Yb_n) plots, with inflexions in the MREE part or with folded patterns within a Sm-Eu maximum (315-253). Pyroxenes have joint Zr-Hf-Ti depressions in four cases of five (Fig. 7, *c*), whereas pyroxene spidergrams for lherzolites show only a weak Zr dip (Fig. 7, *d*). Pyroxenes from

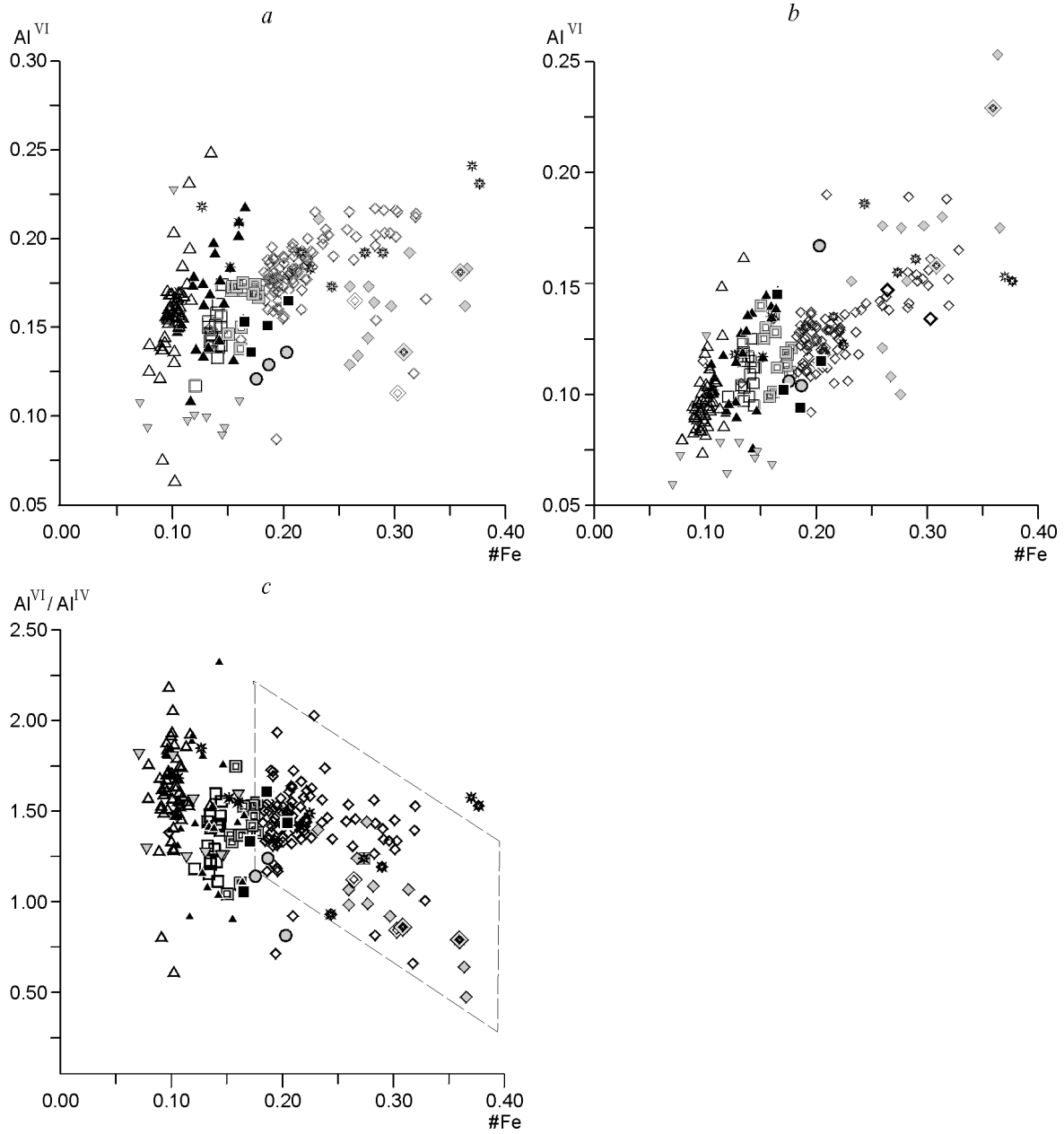

Fig. 5. Al^{VI}, Al^{IV} and Al^{VI}/Al^{IV} ratios vs. Fe# (degrees of fractionation). For legend see Fig. 2.

garnet lherzolites (Fig. 7, *d*) stand out by their weakly variable humped REE patterns. Their chondrite-normalized TRE [38] generally correspond to clinopyroxenes in common fertile lherzolites.

DISCUSSION

The variability of **black pyroxenite megacrysts** (Figs. 2, 3) is accounted for by a model of fractional crystallization [4, 5, 39]. The degree of fractionation and proportions of precipitates were estimated using partition coefficients for clinopyroxene [40] and garnet (obtained for sample 315-254 by recalculation of $D_{\text{Ga/Cpx}}^{\text{measured}} \times D_{\text{Cpx/melt}}^{\text{experimental}}$). The first approximation is based on recombination of the Rayleigh fractionation equation [39]

$$C_i / C_0 = f^{(D_{\text{solid/melt}} - 1)}$$

Table 1

Selected Analyses of Pyroxenes and Associated Minerals from Pyroxenites of Different Suites

Element	Green pyroxenite	Dark-green pyroxenite	Black garnet pyroxenite		Black pyroxenite		Black kelyphitic pyroxenite	Black ilmenite-phlogopite pyroxenite	
	315-104	315-117	315-254	315-254	315-174	315-167	315-133	315-340	315-340
	Clinopyroxene			Garnet	Clinopyroxene				Phlogo-pite
SiO_2	52.59	51.30	50.73	41.48	49.87	49.55	49.22	49.43	36.91
TiO_2	0.33	0.53	0.63	0.38	1.30	1.49	1.51	1.64	8.41
Al_2O_3	5.07	7.25	7.54	22.62	7.95	8.06	8.90	8.23	15.67
Cr_2O_3	0.77	0.13	0.02	0.05	0.00	0.02	0.00	0.01	0.01
FeO	4.80	7.41	7.57	12.45	8.84	9.24	10.29	8.41	12.32
MgO	19.58	17.40	15.46	17.60	13.20	12.73	9.83	11.87	14.10
CaO	15.10	13.79	15.10	5.07	15.78	15.67	15.83	15.46	0.21
Na_2O	1.06	1.62	1.97	0.11	2.50	2.61	3.31	3.42	0.11
K_2O			0.63		1.30	1.49	1.51		6.26
F									0.46
Cl									0.02
Total	99.30	99.43	99.64	99.76	100.74	100.86	100.40	98.47	94.48
Ba	5.161	1.438	2.2532	0.64	4.1234	3.23	24.376	6.788	4374.2
La	1.542	1.016	1.2148	0.054	1.6125	1.83	2.1987	2.007	0.242
Ce	5.237	3.809	4.4049	0.259	6.2239	6.9	8.2583	7.600	0.410
Pr	0.934	0.719	0.88328	0.088	1.2449	1.38	1.6266	1.534	0.055
Nd	4.914	4.139	5.0294	0.971	7.2483	8.52	9.1808	9.814	0.000
Eu	0.546	0.580	0.66828	0.712	0.94705	1.03	1.1357	1.032	0.053
Sm	1.511	1.512	1.7223	1.11	2.4915	2.76	2.9835	2.971	0.000
Gd	1.557	1.789	2.1008	3.75	2.8719	3.39	3.2383	3.329	0.000
Dy	1.321	1.726	1.7544	9.24	2.0861	2.33	2.1453	2.341	0.159
Ho	0.240	0.316	0.32314	2.49	0.34102	0.35	0.3398	0.348	0.009
Er	0.566	0.738	0.70756	8.54	0.64738	0.631	0.61077	0.605	0.000
Yb	0.392	0.485	0.43588	9.35	0.29972	0.269	0.26697	0.174	0.000
Lu	0.045	0.054	0.05598	1.37	0.0325	0.028	0.02818	0.024	0.000
Hf	0.488	0.648	0.92	1.117	1.8	2.31	3.62	2.712	0.200
Ta	0.001	0.005	0.029	0.255	0.053	0.033	0.059	0.113	0.390
W	0.054	0.072	0.023	0.207	0.027	0.015	0.005	0.113	0.144
Pb	0.083	0.052	0.189	0.107	0.097	0.164	0.157	0.000	0.000
Th	0.038	0.022	0.023	0.0079	0.025	0.023	0.031	0.038	0.014
U	0.008	0.005	0.0136	0.0091	0.0066	0.0044	0.0081	0.004	0.000
Sc	25.49	17.61	22.31	89.8	16.28	13.39	14.33	13.06	5.80
V			390.94		534.38		235.45		
Co	29.43	35.15	52.8	62.5	51.9	54.8	43.6	34.85	322.23
Cu	3.78	5.96	22.1	8.4	13.13	12.52	10.23	6.36	22.13
Zn	20.83	33.13	43.3	26.6	52.7	64.7	57.3	35.51	57.34
Ge	1.59	1.49	1.31	2.13	1.24	1.45	0.467	1.03	0.48
Rb	0.15	0.12	0.236	0.089	0.363	0.151	0.489	0.44	707.39
Sr	64.61	52.27	63.8	1.54	100	112	133	72.982	149.92
Y	5.40	7.55	7.28	46.2	7.39	8.57	7.1	8.59	0.29
Zr	12.80	16.50	24.6	27.9	48.2	46.4	94.9	57.16	2.92
Nb	0.197	0.147	0.278	0.109	0.379	0.266	0.253	0.660	3.015
Mo	1.0144	0.19908	0.11	0	0.022	0	0.001	0.32437	0.28764
Cs	<0.01	<0.01	0.0027	0	0.0047	0.0049	0.0039	0.01	9.13

Table 1 **(continued)**

Phlogopite-kaersutite pyroxenite		Mega-cryst	Plagio-clase cpx	Plagioclase-garnet clinopyroxenite		Gneissic basic cumulate		Cr-Di webs-terite	Cr-Di websterite with garnet		
315-440	315-440	315-414	327-3	327-2	327-2	327-5	327-5	315-251	315-252	315-252	315-252
Cpx	Phl	Kaer	Cpx		Opx	Cpx	Opx	Cpx		Ga	Opx
51.04	36.82	42.61	47.05	49.03	51.85	48.99	52.12	51.79	51.87	42.35	54.26
1.00	8.48	4.24	1.71	1.13	0.18	0.59	0.11	0.28	0.37	0.18	0.14
6.25	13.68	12.49	9.23	6.65	4.73	8.22	6.13	6.47	5.99	23.13	4.07
0.42	0.53	0.28	0.02	0.01	0.02	0.01	0.00	0.80	0.29	0.34	0.17
4.82	8.15	7.48	9.80	9.29	19.51	7.17	15.33	3.32	3.47	7.84	6.57
13.47	16.71	14.92	9.82	11.70	23.39	12.49	26.64	16.00	16.12	20.90	32.79
20.44	0.00	9.42	20.78	20.01	0.54	21.10	0.44	18.40	18.52	4.97	0.94
1.67	0.37	3.27	1.31	1.59	0.06	1.42	0.05	1.95	2.01	0.03	0.20
0.00	9.54	1.69	1.71	1.13		0.59		0.28	0.37		0.01
99.11	94.27	96.40	101.43	100.54	100.28	100.59	100.82	99.29	99.01	99.74	99.15
5.070	11535	99.463	7.9195	24.96	64.44	17.81	9.89	1.0019	1.4749	0.071	12.97
2.261	0.286	10.655	11.021	8.55	3.78	6.43	0.248	1.4092	1.7922	0.020	0.369
16.020	0.986	35.444	48.651	45.75	15.98	28.95	0.612	4.5836	5.8659	0.163	1.28
3.851	0.185	6.288	8.9308	10.05	3.13	5.44	0.088	0.82029	1.0187	0.060	0.245
24.997	0.722	36.743	41.592	58.22	17.09	27.54	0.423	4.1811	5.2439	0.673	1.47
0.640	0.066	2.909	1.8579	3.6	1.02	1.47	0.029	0.46911	0.61261	0.562	0.131
6.500	0.000	8.960	6.7697	15.04	4.02	5.72	0.096	1.2139	1.5959	0.802	0.457
6.130	0.212	8.847	3.49	13.09	3.76	3.79	0.097	1.38958	1.7317	2.616	0.596
4.470	0.266	5.370	1.102	8.88	2.63	1.75	0.069	1.1215	1.0999	6.221	0.64
0.821	0.040	0.840	0.15886	1.52	0.486	0.249	0.012	0.21248	0.18288	1.626	0.134
1.949	0.058	1.676	0.27808	3.64	1.19	0.486	0.031	0.4814	0.35125	5.026	0.368
1.536	0.000	0.857	0.14418	2.74	1.09	0.275	0.031	0.33102	0.192262	4.922	0.394
0.249	0.171	0.136	0.01782	0.38	0.169	0.034	0.005	0.04617	0.02337	0.678	0.061
2.177	0.164	4.104	2.25	10.85	2.55	3.84	0.311	0.433	0.594	0.426	0.514
0.000	0.293	3.506	0.143	0.086	0.173	0.074	0.293	0.027	0.204	0	0.091
0.000	0.000	0.076	0.331	1.22	1.12	0.509	0.185	0.165	0.214	0.022	0.436
0.023	0.031	0.095	0.245	0.184	0.059	0.102	0.012	0.035	0.102	0.004	0.019
0.004	0.010	0.017	0.0349	0.053	0.021	0.048	0.008	0.0125	0.0273	0.009	0.015
54.95	10.34	17.94	49.1	54	35.34	10.12	3.84	22.05	20.4	32.51	9.52
			948.09					294.23	346.45		
29.34	212.79	174.82	54.9	35.6	78.5	47.2	133	29.3	29.3	32.22	111
4.2272	14.89	10.59	12.25	8.18	5.97	5.72	2.05	8.71	11.86	0.66	4.56
35.72	20.68	37.89	106	80.3	226	24.3	92.7	15.22	17.23	9.37	424
1.40	0.32	0.96	1.4	1.53	2.15	0.795	0.99	1.02	1.16	2.25	1.69
0.22	580.90	6.67	0.651	0.551	1.53	0.424	0.369	0.065	0.104	0.22	0.638
141.44	357.33	599.37	80.3	51.4	106	119	16.38	94.9	82.7	0.32	13
21.53	1.04	19.60	2.94	28.8	12.55	5.47	0.356	4.75	3.84	27.46	3.91
53.23	1.80	114.39	138	238	84.5	95.9	8.58	13.05	24.2	24.95	15.95
0.185	1.465	51.581	1.14	0.956	2.31	0.393	0.354	0.336	1.47	0.174	0.358
0.17505	0.8493	0.3929	0.045	0	0	0	0	0.041	0.021	0.29159	0
0.00	1.90	0.04	0.0148	0.0007	0.0118	0.0015	0.0071	0.0021	0.0029	<0.01	0.0094

Note. Major oxides, F, and Cl are determined by EMPA, other elements by ICP-MS.

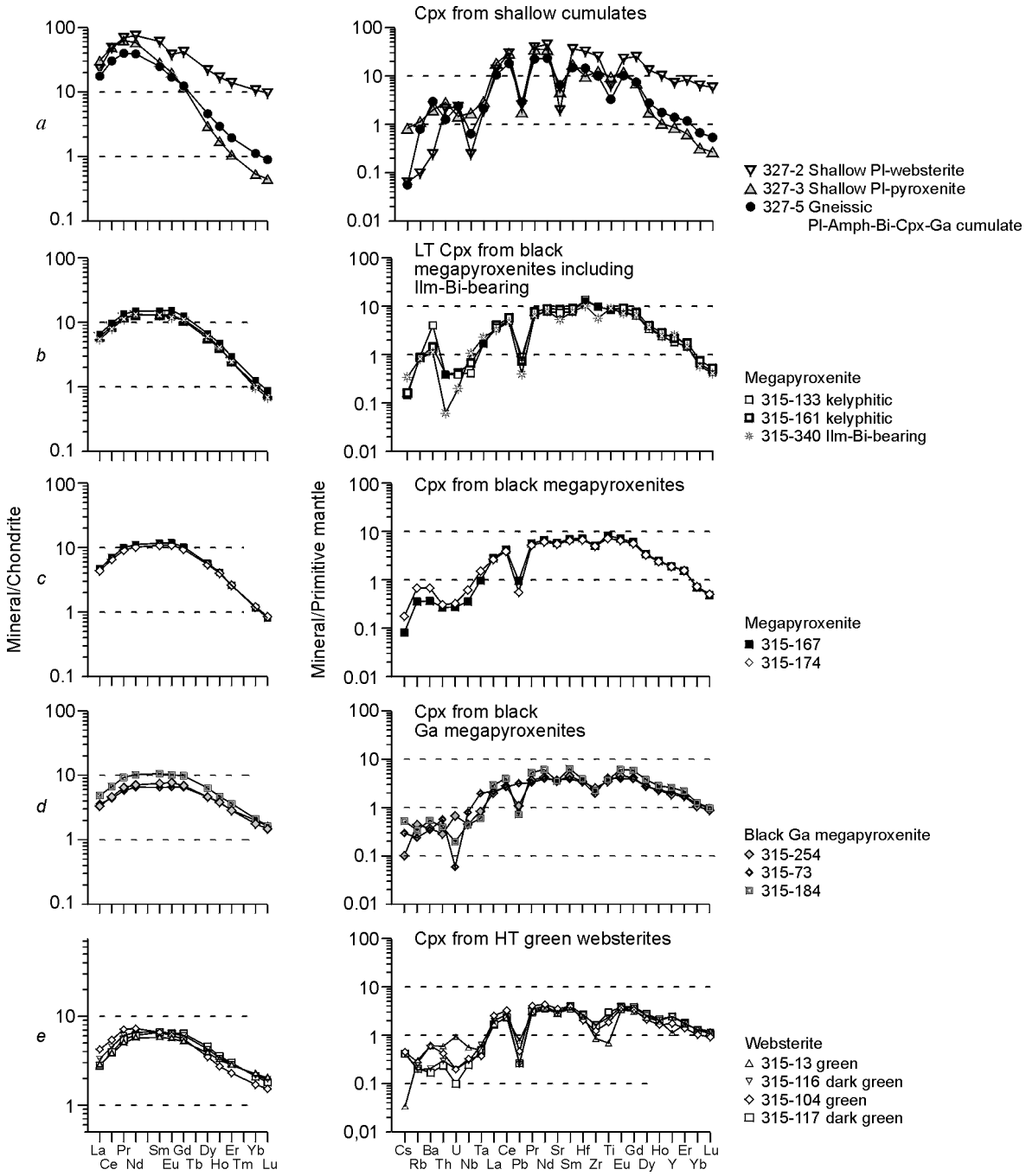

Fig. 6. Chondrite-normalized REE patterns [61] and spidergrams normalized to primitive mantle [38] for clinopyroxenes from HT megapyroxenites xenoliths and from MT Cr-bearing pyroxenites and lherzolites. Enrichment and contrasts grow upwards (from *e* to *a*), especially in shallow cumulates; all diagrams show Pb, Zr, and Th dips; U and Nb are highly variable. See text for explanation.

for LREE where the effect of garnet is negligible

$$\ln f = (C_i/C_0)/(D_{\text{Cpx/melt}} - 1), \quad (1)$$

where C_i is the concentration of component in clinopyroxene at the i-th step of crystallization, $D_{\text{Cpx/melt}}$ is partition coefficient. Having solved (1) for D and suggesting D as D_{bulk}

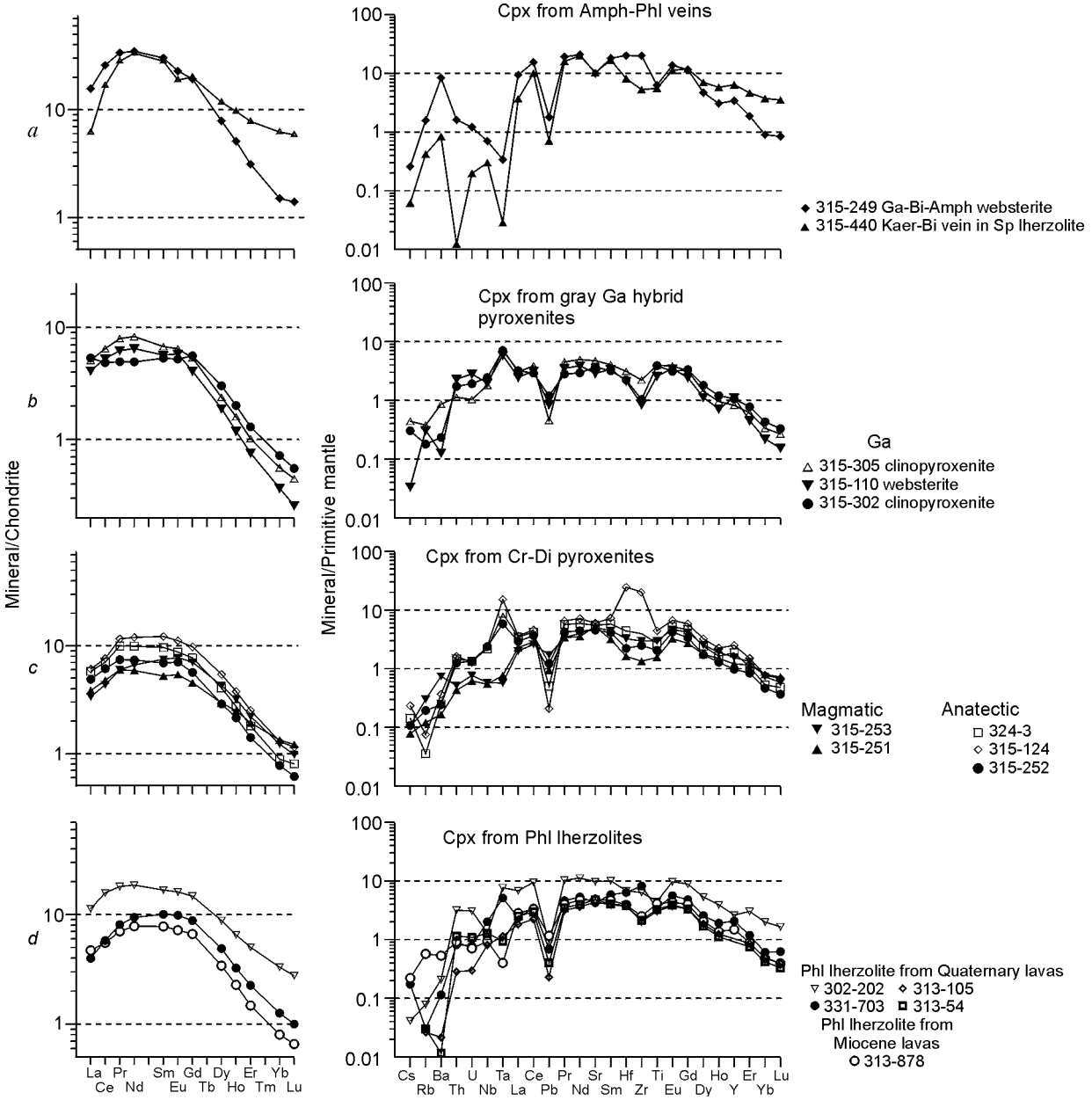

Fig. 7. Chondrite-normalized REE patterns [61] and spidergrams normalized to primitive mantle [38] for clinopyroxenes from hybrid pyroxenite veins and lherzolites. See text for explanation.

$$D_{\text{bulk}} = \ln (C_i / C_0) / \ln (f) + 1, \tag{2}$$

the bulk partition coefficient ($D^i_{\text{solid/melt}}$) can be found for several MRE and HRE elements. By definition

$$D^i_{\text{solid/melt}} = D_1 \cdot M_1 + D_2 \cdot M_2 + \ldots + D_n \cdot M_n, \tag{3}$$

which allows us to find the proportion between phases (M_n) by writing (3) for most reliably determined elements whose number corresponds to the number of phases and by solving the system of equations. Small-step interactive variation of proportions of two phases (Cpx and Ga), for instance in Excel spreadsheets, produces a perfect fit of model TRE patterns to the natural spectra. In the general case this is a simple iteration procedure in which the phase proportion may be determined with definite accuracy by calculating rms error (R) for certain elements. Unlike the binary diagrams, the error is as low as <1% (under the assumption of negligible temperature variations of the partition coefficients).

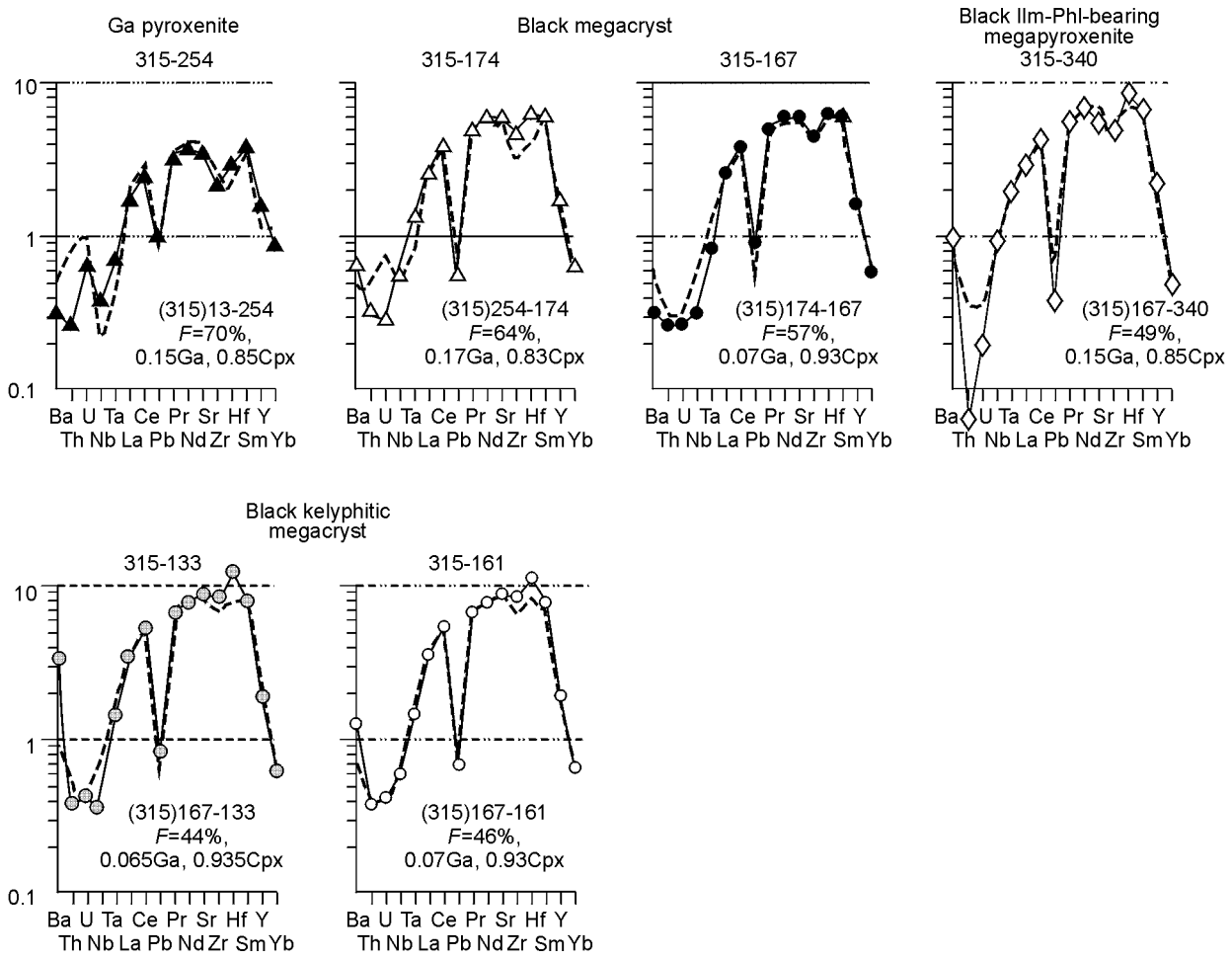

Fig. 8. Model REE patterns for pyroxenes in pyroxenite megacrysts. Solid lines are for analyzed and bold dashed lines for modeled TRE patterns.

The natural and model spectra of black pyroxenite megacrysts characteristically show smooth plots (Fig. 8). Modeling of simple fractionation for HT green websterites as a starting composition failed. Starting with the least HT garnet pyroxenite (sample 315-254, Fig. 8), the degree of fractionation (amount of the remaining liquid) decreases from ~70–57% in the first group (three first diagrams in Fig. 8), to 50–45% in monomineral clinopyroxenites and ilmenite-phlogopite-bearing phases, and to 40% in kelyphitic pyroxenites. The proportions of garnet vary discontinuously (6.5–5% or ~15–17%) and fall at lower temperatures. Higher model Ta and Nb abundances require crystallization of 10 to 20% ilmenite (which is inconsistent with the TiO_2 balance) or higher amounts of Ti biotite or kaersutite at certain fractionation stages. On the other hand, ilmenite-bearing pyroxenites with elevated HFSE cannot be produced by continuous fractionation of less differentiated varieties but rather require selective dissolution (up to 10% of earlier precipitated ilmenite) or assimilation of kaersutite- or biotite-bearing metasomatites. Note that $D_{Ilm/melt}$ are taken high relative to [41]: 14 for Ta and 7.7 for Nb (determined according to [42] using $D_{Cpx/melt}$ from [40]). The coefficients of 1.7 and 2.0 [41] correspond to a higher proportion of HSFE concentrators. The TiO_2 balance suggests the participation of mica or amphibole, however, at still higher fractionation degrees.

In our simplified model, partition coefficients are independent of melt temperature and composition. The temperature dependence is simple and strong for garnet [43] and more complicated (controlled mostly by Al^{IV}) for clinopyroxene [44], but is weaker in the high-temperature range anyway. Fractionation with variable partition coefficients was discussed in [5], where the initial coefficients were estimated from the compositions of similar Ti-augite megacrysts. The pyroxenes from Nógrád, Hungary, are enriched in Zr, Hf, and Ta but depleted in Ti, Nb, and Sr; they crystallized jointly with plagioclase (Sr minimum), ilmenite or Ti magnetite (Ti minimum), which

may have influenced the HFSE behavior. Note that lower *D* leads to flatter HREE patterns for more strongly fractionated varieties.

Complication of the model neither changes much the calculated phase proportions nor decreases the fractionation degrees, as the *D* decrease associated with a ~250° temperature drop is 1.1–1.8-fold for REE and 3-4-fold for HFSE [5]. Lower-Zr and Hf model compositions support lower effective partition coefficients for HFSE (Fig. 8).

Modeling for **HT hybrid green websterites** implies interaction of the primary picrite-basalt melts with wall rock peridotites. Of several explanations [39], one in [45] appears the most plausible. Low Gd/Yb_n suggest that the melts were assimilating a solid, most likely peridotite or its highest soluble phases (garnet and clinopyroxene), but the proportion of garnet must be higher then in lherzolites. We selected equal amounts of these phases and $R = 0.15$ (A/C assimilation-crystallization ratio) and clinopyroxene as the only crystallizing phase. At the fractionation degree about 0.5–0.7, the model curves generally fit the natural distribution, except for LILE and some HFSE. Fitting of other parameters can be achieved by adding hydrous minerals and crystallizing small amounts of ilmenite.

The origin of these rocks may be also modeled by melting of metasomatic substrate, but this is associated with much stronger TRE variations. The mirror-like LREE patterns of the clinopyroxenes mean crystallization of the parent melts accompanied by dissolution and fractionation of HFSE-bearing phases.

Shallow black plagioclase clinopyroxenites and websterites (*8* and *13* in Fig. 2) were considered end-member differentiates of basalt melts responsible for the formation of megacrysts [7, 11, 16, 18, 46], but this interpretation was disproven by numerical modeling. Considerably higher LREE and the U shape of the HREE branch are rather typical of low-degree melting with a high percentage of garnet (>5%) (e.g. garnet granulites). The bulk lower crust does not show source melt fractionated and high-TRE patterns [47]. Low HFSE and Pb abundances indicate precipitation of oxide phases and sulfides, which is typical of island-arc melts [48]. Varieties with idiomorphic plagioclase have weak Eu minimums (327-2), which are, however, poorly pronounced in some plagioclase-rich rocks with pyroxenite veins (e.g. 327-5) where clinopyroxene can crystallize in injections or as an earlier (as in 327-3) phase source melt. As the presence or absence of Eu anomalies may depend on oxidation conditions [49], a well-defined Sr minimum remains the only evidence for plagioclase fractionation. Possible contamination of primary melts with lower crust material during the formation of plagioclase pyroxenites (reflected in elevated Ba, Th, and U abundances) is confirmed by their isotopic composition similar to EMI or EMII unlike the megacrysts in which it is close to the Earth's average bulk composition [6]. Plagioclase pyroxenites can exist as veins in crustal granulites or as deep cumulate sills underplating the lower crust. Strictly speaking, they hardly can be cognate with the basalts of this stage of volcanism. Comparison of xenoliths of other stages from different regions shows that shallow cumulates vary at each volcanic stage. The < 5–7% proportions of remaining liquid in fractional crystallization of high-Fe# varieties, estimated using the LILE of the same starting source melt, appear doubtful. Alternative scenarios are (1) assimilation of crustal material by basalt melts in magmatic chambers as a result of roof detachment, oxidation, and precipitation of oxide phases; (2) anatexis and mixing of partial melts with injected fractionated basaltic magmas; (3) crystallization from earlier basaltoid or andesite-basalt magma. The homogeneous composition and typical cumulate structures, without division into leucocratic and melanocratic components, evidence rather for minor intrusions contaminated to different degrees than for larger layered plutons at the crustal base.

Folded REE patterns of **MT hybrid gray pyroxenites** (Fig. 7, *b*, *c*), observed earlier in Ti phlogopites [37], indicate *selective dissolution* of minerals. The pyroxenites may have been produced by multi-stage melting, including removal of a phase (clinopyroxene) at the first stage, remelting of wall-rock minerals by interaction with fluid-saturated melt at the second stage, and precipitation of the phase with folded spectra at the final stage. The plausibility of such a process is supported by U-shaped REE patterns of the solution obtained after dissolving the margins of clinopyroxene grains in sample 315-302, though the pyroxene itself does not show anything unusual in its MREE pattern. The dissolved aggregate is a mixture of decomposed interstitial glass and kelyphytic rims, and REE concentrations in it are higher than in clinopyroxene. Hence, the portion of remelted interstitial material (mineral-forming at the final stage) is very high for melts producing two-folded REE patterns. We modeled the bulk composition of the source as containing 10% intergranular material, 75% clinopyroxene, and 15% garnet. Melting of garnet pyroxenite with 85% Cpx — 15% Ga in the restite leads to crystallization of pyroxene with a REE pattern similar to 315-305 (Fig. 7, *b*). The radiated HREE patterns are caused by variable amounts of garnet (Fig. 9, *b*) in the restite during the formation of the parent melt. Increasing clinopyroxene is indicated by intersection of REE plots. Melting of peridotites with equal proportions of garnet and clinopyroxene and increasing modal olivine is associated with REE increase with the plots remaining conformal (Fig. 9, *c*).

Cr-Di veins are formed from melts produced by fusion of lherzolites (<1.2% *partial melting* according to

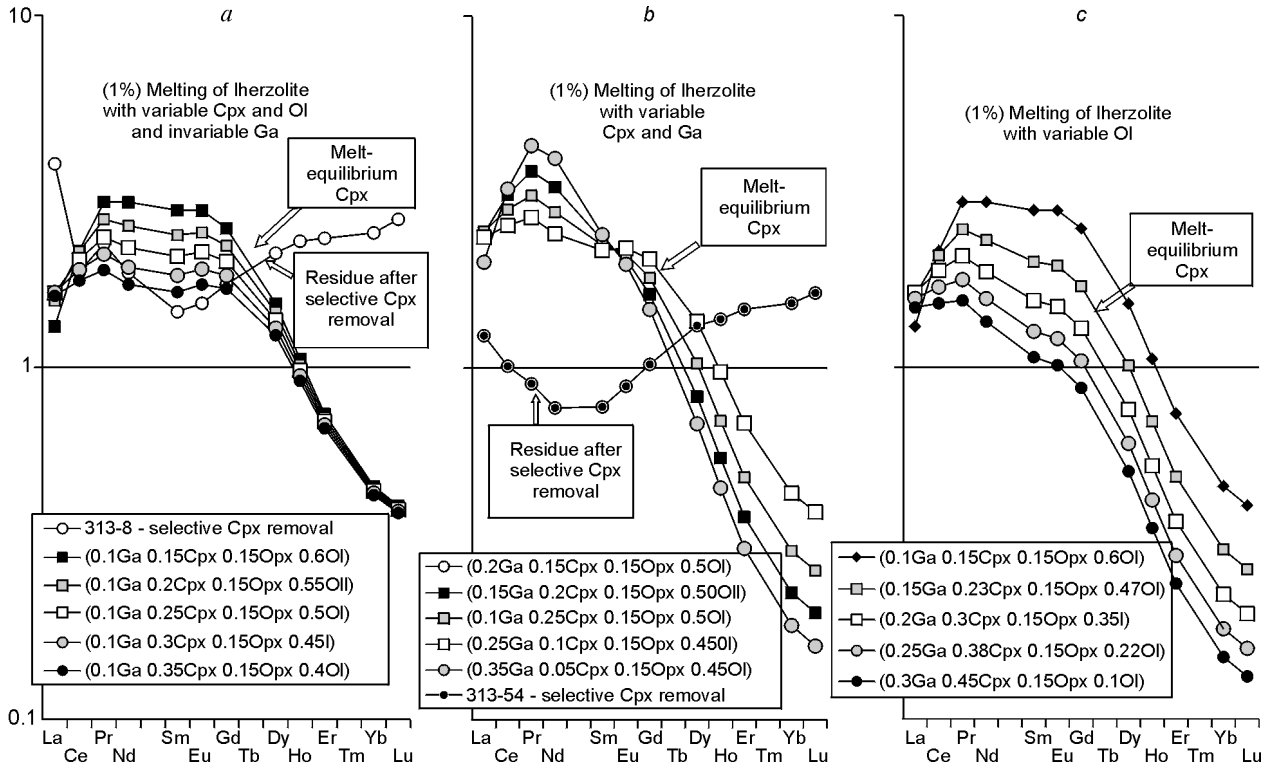

Fig. 9. Melting of garnet lherzolite with variable proportions of reagent minerals (a model). *a* — with invariable amounts of garnet and orthopyroxene and variable amounts of clinopyroxene and olivine; *b* — with invariable amounts of olivine and orthopyroxene and variable amounts of garnet and clinopyroxene; *c* — with invariable garnet/orthopyroxene ratio and variable amounts of olivine. REE patterns belong to rock from which we removed 10 % clinopyroxene and to clinopyroxenes in equilibrium with melts obtained at different proportions of minerals (controlled by melt geometry).

modeling). An ideal field of elements in a clinopyroxene precipitate from partial melts of a primitive mantle source is approximated by a smooth arc in the spidergram plotted in the order of incompatibility [50]. Real diagrams (Fig. 7, *c*, *d*), however, display considerably varying HFSE and Pb contents, occasionally with mirroring fluctuations. The behavior of Ta and Nb (some samples show distinct Ta peaks, e.g. Fig. 7, *c*) may be controlled by ilmenite, but the absence of sharp Ti peaks rather suggests the participation of amphibole or phlogopite. Flatter peaks correspond to the melting of kaersutite, an HFSE concentrator [41]. A Zr-Hf maximum in one sample (315-124), mirroring relative to other samples, may be due to dissolution of accessory zircon [51], ilmenite, rutile, or other HFSE concentrators. The interpretation is difficult, as the trace element geochemistry of accessories in peridotite and mantle veins has been so far poorly known. The TRE composition and trace-element patterns of clinopyroxenes and low-degree equilibrium partial melts might be influenced by layers at grain contacts [52–54]. Flat Zr-Hf-Ti dips of pyroxenes in Cr-Di veins are associated with fractionation of garnet-spinel and orthopyroxene from the parent melts. Slope variations of HREE plots are controlled by the amount of garnet during melting and fractionation. The steep left part of the REE plot for 315-253 (Fig. 7, *c*) may indicate remelting of an LREE-depleted substrate, e.g. a mixture of dunites and garnet clinopyroxenites (contact zones of mantle magmatic systems) which perfectly fits the model composition. Weak REE minimums (near Sm) (Fig. 7, *c*) shown by many Cr-Di pyroxenites, same as in lherzolite associations, may record depletion of the primary bulk composition during selective removal of clinopyroxene (Fig. 9, *a*).

Remelting of pyroxenites must correspond to a ~2–5% partial melting. The degree of melting of metasomatites depends on the proportion of hydrous phases and is most often as low as 0.1–1%. Because of very low viscosity, the fluid-saturated melt must be rapidly removed or assimilated by the intruding magma.

Cr-Di veins may form either by segregation of interstitial melts or by remelting of earlier veins and metasomatites. Elevated HFSE concentrations in the latter indicate remelting of kaersutite veins, and relative LILE enrichment is associated with melting of mica aggregates. Additional strong differentiation of metasomatites

dissolved by magmatic liquid may be suggested for gray low-Cr garnet websterites (Figs. 2 and 7, *b*). Veins with high Na, Al, Ti, and incompatible trace elements in pyroxenes may be products of repeated low-degree melting of anatectic pyroxenites, their differentiates, and metasomatites, favored by the presence of incompatible elements in the interstitial space (glasses or their fine-grained recrystallized aggregates) [53, 54].

Interstitial lherzolite partial melts also bear signature of differentiation. Higher REE abundances in a Cr-diopside from a phlogopite lherzolite sample (Fig. 7, *d*, sample 302-202, Quaternary Kandidushka volcano), which is higher-Fe# relative to other lherzolites, may be referred to impregnation by a strongly differentiated basaltic melt [55, 56]. The melt must have evolved in an isolated vein system, as is suggested by the absence of Fe#-dependent interstitial differentiation trends, possibly because of high Mg-Fe diffusivity. The Fe-Ti trends reported in [46] are rather associated with temperature increase [57] and thus cannot be interpreted as differentiation trends. Phlogopites from lherzolites [46 and our data] also have exotic mirror REE patterns possibly produced by fractional crystallization with selective melting of wall-rock clinopyroxene. The Ce minimums observed in the Vitim *lherzolite garnets* [58] may be controlled by accessory zircon [51] or apatite.

PROCESSES IN MANTLE VEIN SYSTEMS

Thus all types of mantle pyroxenites, as well as many peridotites, show signature of dissolution of earlier material, which is an essential evolution law in vein differentiation. It is especially so in the conditions of abrupt $T(P)X$ fluctuations during repeated melting pulses, when the appearance of a free fluid phase causes selective dissolution of minerals and incompatible-element enrichment of melts. Ilmenites in black and hybrid pyroxenite xenoliths most often fill the connected fluid cavities and are often coated with brown glassy films [16] compositionally similar to glass in lherzolites crystallized from fluids or fluid-saturated melts [54, 55].

Repeated melting/crystallization cycles favor rapid evolution of vein material, which becomes enriched in incompatible elements or mineralized by fluids.

Most of the studied mantle xenoliths with cumulate structures, channels or voids are too fine grained to have been associated with long-existing melt conduits. Signs of crystallization in open space (druses, voids, etc.) are observed only in HT megacrysts. Black pyroxenites rather form small pegmatitic sills and vertical magmatic veins in the lower crust and mantle, judging by broad temperature (1350 to 950°) and pressure (27 to 12 kbar) ranges and polybaric fractionation trends. These vein systems form by hydraulic fracturing mechanics [59] accompanied by rapid differentiation of the filling melt and become feeding systems for future eruptions. New conduits may form as a “dike-in-dike” or along contacts between peridotites and earlier pyroxenite veins. At first, rising melts may use pores left by crystallization of liquid that often remains in cumulate mantle xenoliths.

Moderate variations of Fe# indicate that its content in parent melts was partly buffered at the initial stage by host peridotites, most likely, by the AFC (assimilation-fractional crystallization) mechanism [45]. Progressive assimilation decrease at lower temperatures, as well as crystallization of pyroxenes and accessories, controlled Cr_2O_3 decrease. The poikilitic textures of some varieties and exsolution lamellae on the periphery of large clinopyroxene grains attest to fractionation in the conditions of repeatedly supplied small fractions of magmatic liquid which accounts for broad compositional variations of the 1350–1250 °C melts.

The history of the vein system beneath the Vitim plateau at the initial volcanic stage can be reconstructed using xenoliths of different ages, as we tried in a special paper [57]. However, its multi-stage evolution is only implicitly indicated by signs of brittle deformation in black megacrysts and mylonitic textures of some Cr-Di pyroxenites, whereas different pyroxenites show almost no contact relationships.

Intrusion of major batches of magma was preceded by metasomatism and partial melting that produced anatectic Cr-Di websterites. Amphibole-phlogopite veins have a K-Ar age of 46 Ma, which is close to the Sm-Nd age of lherzolites [60]. The specific REE patterns of Cr-Di pyroxenites and their Sr-Nd trends attest to an origin by remelting of metasomatites rather than simple segregation of melts. The relatively high-temperature iron varieties with HFSE peaks from remelted kaersutites apparently originated at the crystallization front in a vein system formed by rising plume melts. Differentiation within this system is indicated by correlated trends of temperature-dependent Cr_2O_3 decrease (to 0.1%) and CaO growth [57].

Mid-temperature giant-grained hybrid pyroxenites may owe their origin either to remelting of hydrous metasomatites from the vein system produced by intrusion of the first batches of hydrous plume magma or to hybridization of strongly differentiated melts.

The HT giant-grained pyroxenite suite apparently formed prior to the main portion of plume basalts. This earlier pulse produced a fracture in the upper part of the magmatic chamber at a depth about 85 km (27 kbar) in which clinopyroxene and garnet precipitated and essentially orthopyroxene rocks formed in near-contact zones. High-temperature green hybrid Cr websterites may have formed in isolated apophyses within hot outer contacts.

The melts accumulated volatiles during partial fractionation and moved to shallower depths forming intermediate chambers near the garnet/spinel transition, then further to the spinel facies, and finally to the crustal base. Thus the ascent of melts was accompanied by differentiation and formation of metasomatites. Oxidation and accumulation of volatiles favored crystallization of pegmatitic pyroxene blocks, their decomposition by fluids, like in pegmatites, and partial replacement with the formation of ilmenite and phlogopite in gaseous blebs and channels. Once penetrated to the crust, the residual melts became oxidized and crystallized Ti magnetite and then HT feldspar. The parent melts of the giant-grained suite were detached from the main body of basaltic magma and may have formed pegmatitic sills and vertical conduits for future erupting melts.

CONCLUSIONS

1. Clinopyroxene megacrysts were produced by fractionation of basalt melt, isolated (frontal?) from the main body of basaltic magma, in a polybaric vein system at the pre-eruption stage.

2. The fractionation occurred by pulses and was accompanied by dissolution of earlier phases.

3. High-temperature and volatile-rich basaltic melts are strongly hybridized with peridotite material in the mantle and with basic gneisses in the lower crust.

4. Melts that crystallize lherzolite minerals and most of Cr-Di veins form by ~1% partial melting of the primitive upper mantle lherzolite.

5. Cr-Di and hybrid veins often originate during melting of metasomatites with a variable phase composition and specific (including U-shaped) REE patterns and form connected vein systems.

We wish to thank Prof. J. Klerkx for promoting ICP-MS studies in the Royal Museum for Central Africa, Prof. A.I. Almukhamedov (Irkutsk) for constructive criticism, and the team of analysts from the EMPA laboratory in UIGGM (Novosibirsk). Thanks are extended to M.A. Kalmanovich, S.V. Kanakin, and I.N. Ryazanov for field collaboration in 1986-1988. Acquisition of large sample collections is due to participation of S.V. Esin, Yu.D. Litasov, and others. Many analyses were obtained through the project “Upper mantle petrology in rift zones” run by a temporary team of young scientists at the United Institute of Geology, Geophysics and Mineralogy in 1990-1992.

The study was supported by grants 94-05-17103a and 99-05-65688 from the Russian Foundation for Basic Research.

REFERENCES

1. Lambert, R.S., V.E. Chamberlain, and J.G. Holland, Ferro-andesites in the Grande Ronde basalt — their composition and significance in studies of the origin of the Columbia river basalt group, *Can. J. Earth Sci.*, **32**, 4, 424–436, 1995.

2. Farnetani, C.G., M.A. Richards, and M.S. Ghiorso, Petrological models of magma evolution and deep crustal structure beneath hotspots and flood basalt provinces, *Earth Planet Sci. Lett.*, **143**, 1–4, 81–94, 1996.

3. Chalokwu, C.I., N.K. Grant, A.A. Ariskin, and G.S. Barmina, Simulation of primary phase relations and mineral compositions, *Contrib. Mineral Petrol.*, **114**, 539–549, 1993.

4. Neal, C.R., and J.P. Davidson, An unmetasomatized source for the Malaitan Alnoite (Solomon Islands) petrogenesis involving zone refining, megacryst fractionation, and assimilation of oceanic lithosphere, *Geochim. Cosmochim. Acta.*, **53**, 8, 1975–1990, 1989.

5. Dobosi, G., and G.A. Jenner, Petrologic implications of trace element variation in clinopyroxene megacrysts from the Nógrád volcanic province, north Hungary: a study by laser ablation microprobe-inductively coupled plasma-mass spectrometry, *Lithos*, **46**, 4, 731–749, 1999.

6. Ashchepkov, I.V., and L. André, Deep seated differentiation of the mantle melts: evidence from Vitim pyroxenite xenoliths, *Earth Planet. Sci. Lett.*, 2001.

7. Ashchepkov, I. V., L. André, K.D. Litasov, and V.G. Malkovets, Origin and evolution of mantle melts beneath Vitim Plateau, *Extended Abstr., Sixth Intern. Kimberlite Conf.*, 17–19, Novosibirsk, 1995.

8. Frey, F.A., The origin of pyroxenites from the Lake Crater, Oahu, Hawaii: trace element evidence, *Amer. J. Sci.*, **280**A, 427–449, 1980.

9. Liotard, J.M., D. Briot, and P. Boivin, Petrological and geochemical relationships between pyroxene megacrysts and associated alkali basalts from Massif Central (France), *Contrib. Mineral. Petrol.*, **98,** 81–90, 1988.

10. Akinin, V.V., M.F. Roden, D. Francis, J. Apt, and E. MollStalcup, Compositional and thermal state of

the upper mantle beneath the Bering Sea basalt province: Evidence from the Chukchi Peninsula of Russia, *Can. J. Earth Sci.*, **34**, 6, 789–800, 1997.

11. Ashchepkov, I.V., and L. André, Vein system beneath the Vitim plateau: mechanism of fractionation and relationships with basaltic melts, *J. Conf. Abstr.*, **1**, 1, 25, 1996.

12. Wilshere, H.G., J. E. Pike, C.E. Meyer, and E.C. Schwarzman, Amphibole-rich veins in lherzolite xenoliths, Dish Hilll and Deadmen Lake, California, *Amer. J. Sci.*, **280**A, 576–593, 1980.

13. Irvine, A.J., Petrology and geochemistry of composite ultramafic xenoliths in alkaline basalts and implications for magmatic processes within the mantle, *Ibid.*, 389–426.

14. André, L., and I.V. Ashchepkov, Acid leaching experiments on the mantle derived Vitim pyroxenites: implications for the role of clinopyroxenes in the mantle processes, in *Petrology and geochemistry of magmatic sites of rocks in the continental and oceanic crust*, ed. D. Demeiffe, 321–345, Publ. Université Libre de Bruxelles, Royal Museum for Central Africa, Tervuren, 1996.

15. Kovalenko, V.I., A.I. Tsepin, D.A. Ionov, and I.D. Ryabchikov, A garnet-clinopyroxene druse as an example of fluid crystallization in the mantle, *Dokl. AN SSSR*, **296**, 5, 1224–1228, 1985.

16. Litasov, K.D., and I.V. Ashchepkov, Ilmenite megacrysts and ilmenite-bearing pyroxenites from alkaline basalts of the Vitim plateau, *Geologiya i Geofizika (Russian Geology and Geophysics)*, **37**, 7, 100–111(97–108), 1996.

17. Nixon, P.H., and F.R. Boyd, Garnet bearing lherzoliotes and discrete nodule suites from the Malaita alneite, Solomon Islands, S.W. Pacific, and their bearing on oceanic composition and geotherm, in *The mantle sample: Inclusions in kimberlites and other volcanics*, eds. F.R. Boyd and H.O.A. Meyer, 400–423, AGU, Washington, 1989.

18. Ashchepkov, I.V., *Mantle xenoliths of the Baikal rift* [in Russian], 160 pp., Nauka, Novosibirsk, 1991.

19. Lindnsley, D.H., Pyroxene thermometry, *Amer. Miner.*, **68**, 93, 335–346, 1983.

20. Bertrand P., and J.C.-C. Mercier, The mutual solubility of coexisting ortho- and clinopyroxene: toward the absolute geothermometer for the natural system? *Earth Planet. Sci. Lett.*, **76**, 109–122, 1985.

21. Brey, G.P., and T. Köhler, Geothermobarometry in four phase lherzolites II: new thermobarometers and practical assessment of using thermobarometers, *J. Petrol.*, **31**, 1353–1378, 1990.

22. Nickel, K.G., and D.H. Green, Empirical geothermobarometry for garnet peridotites and implication for the nature of lithosphere, kimberlites and diamonds, *Earth Planet. Sci. Lett.*, **73**, 158–170, 1985.

23. Ashchepkov, I.V., N.L. Dobretsov, and M.A. Kalmanovich, Garnet lherzolites from alkalic picrites and basanites of the Vitim plateau, *Dokl. AN SSSR*, **302**, 2, 417–420, 1988.

24. Mercier, J.-C.C., Single-pyroxene thermobarometry, *Tectonophysics*, **70**, 1–37, 1980.

25. Yoder, H.S., and C.E. Tilley, Origin of the basalt magma: an experimental study of natural and synthetic rock system, *J. Petrol.*, **3**, 342–532, 1962.

26. Nimis, P., and P. Ulmer, Clinopyroxene geobarometry of magmatic rocks: Part 1. An expanded structural geobarometer for anhydrous and hydrous, basic and ultrabasic systems, *Contrib. Miner. Petrol.*, **133**, 314–327, 1998.

27. Nimis, P., Clinopyroxene geobarometry of magmatic rocks, Part 2: Structural geobarometers for basic to acid, tholeiitic and mildly alkaline magmatic systems, *Contrib. Miner. Petrol.*, **135**, 62–74, 1999.

28. Glaser, S.M., S.F. Foley, and D. Gunther, Trace element compositions of minerals in garnet and spinel peridotite xenoliths from the Vitim volcanic field, Transbaikalia, eastern Siberia, *Lithos*, **48**, 263–285, 1999.

29. Ionov, D.A., I.V. Ashchepkov, H.-G. Stosch, G. Witteickschen, and H.A. Seck, Garnet peridotite xenoliths from the Vitim volcanic field, Baikal region — The nature of the garnet spinel/peridotite transition zone in the continental mantle, *J. Petrol.*, **34**, 6, 1141–1175, 1993.

30. Dobretsov, N.L., and I.V. Ashchepkov, Composition and evolution of upper mantle in rift zones (by example of BRZ), *Geologiya i Geofizika (Russian Geology and Geophysics)*, **32**, 1, 5–13(1–8), 1991.

31. Esin, S.V., V.M. Logvinov, and I.V. Ashchepkov, Megacrysts of alumina clinopyroxenes from alkali basaltoids of the Minusinsa Depression, Baikal Rift Zone, and Eastern Sikhote-Alin, *Geologiya i Geofizika (Russian Geology and Geophysics)*, **34**, 7, 101–110(81–88), 1993.

32. Shaw, C.S.J., and J. Eyzaguirre, Origin of megacrysts in the mafic alkaline lavas of the West Eifel volcanic field, *Lithos*, **50**, 5075–5095, 2000.

33. Liu C.-Q., A. Masuda, and G.-H. Xie, Isotope and trace-element geochemistry of alkali basalts and associated megacrysts from the Huangyishan volcano, Kuandian, Liaoning, NE China, *Chem. Geol.*, **97**, 219–231, 1992.

34. Hauri, E.H., T.P. Wagner, and T.L. Grove, Experimental and natural partitioning of Th, U, Pb and other trace elements between garnet, clinopyroxene and basaltic melts, *Chem. Geol.*, **117**, 149–166, 1994.

35. Klemme, S., S.R. van der Laan, S.F. Foley, and D. Gunther, Experimentally determined trace and minor element partitioning between clinopyroxene and carbonatite melt under upper mantle conditions, *Earth Planet. Sci. Lett.*, **133**, 439–448, 1995.

36. Sweeney, R.J., V. Prozesky, and W. Przybylowicz, Selected trace and minor element partitioning between peridotite minerals and carbonatite melts at 18–46 kb pressure, *Geochim. Cosmochim. Acta*, **59**, 18, 3671–3683, 1995.

37. Ashchepkov, I.V., L. André, and K.D. Litasov, Phlogopite in Vitim mantle xenoliths, *J. Conf. Abstr.*, **1**, 1, 29–30, 1996.

38. McDonough, W.F., and S.S. Sun, The Composition of the Earth, *Chem. Geol.*, **120**, 3–4, 223–253, 1995.

39. Rollinson, H.R., *Using geochemical data: evaluation, presentation, interpretation*, 354 pp., Longman Scientific and Technical, J. Wiley & Sons, Inc., New York, 1993.

40. Hart, S.R., and T. Dunn, Experimental cpx/melt partitioning of 24 trace elements, *Contrib. Mineral. Petrol.*, **113**, 1–8. 1993.

41. Zack, T., and R. Brumm, Ilmenite/liquid partition coefficients for 26 trace elements determined through ilmenite/clinopyroxene partitioning in garnet pyroxenites, *7th Intern. Kimberlite Conf., Extended Abstr.*, Cape Town, 986–988, 1998.

42. Foley, S.F., G.A. Jenner, J. Konzett, and R.J. Sweeney, Trace element partitioning in natural phlogopite- and K-richterite-bearing xenoliths from Southern African kimberlites, *6th Intern. Kimberlite Conf., Extended abstr.*, 164–166, Novosibirsk, 1995.

43. Harte, B., and M.B. Kirkley, Partitioning of trace elements between clinopyroxene and garnet: data from mantle eclogites, *Chem. Geol.*, **136**, 1–24, 1997.

44. Blundy, J. D., B. J. Wood, and A. Davies, Thermodynamics of rare earth partitioning between clinopyroxene and melt in the system CaO–MgO–Al_2O_3–SiO_2, *Geochim. Cosmochim. Acta*, **60**, 359–364, 1996.

45. De Paolo, D.J., Trace element and isotopic effects of combined wall rock assimilation and fractional crystallization, *Earth Planet. Sci. Lett.*, **53,** 189–202, 1981.

46. Litasov, K.D., S.F. Foley, and Yu.D. Litasov, Magmatic modification and metasomatism of the subcontinental mantle beneath the Vitim volcanic field, East Siberia: evidence from trace element data on pyroxenite and peridotite xenoliths from Miocene picrobasalt, *Lithos*, **54**, 83–114, 2000.

47. Rudnick, R.L., Continental crust: growing from below, *Nature*, **347**, 711–712, 1990.

48. Tatsumi, Y., and T. Kogiso, Trace element transport during dehydration process in the subducted oceanic crust: 2. Origin of chemical and physical characteristics in arc magmatism, *Earth Planet. Sci. Lett.*, **148**, 207–221, 1997.

49. Drake, M.J., and D.F. Weill, The partition of Sr, Ba, Ca, Y, Eu^{2+}, Eu^{3+} and other REE between plagioclase feldspar and magmatic silicate liquid, *Geochim. Cosmochim. Acta*, **39**, 689–712, 1975.

50. Hofmann, A.W., Chemical differentiation of the Earth: the relationships between the mantle continental crust and oceanic crust, *Earth Planet. Sci. Lett.*, **90**, 297–314, 1988.

51. Belousova, E.A., W.L. Griffin, and S.Y. O'Reilly, Trace element composition and catodoluminiscence properties of kimberlitic zircons, *7th Intern. Kimberlite Conf., Extended abstr.*, Cape Town, 67–68, 1998.

52. Bodinier, J.-L., C. Merlet, R.M. Bedini, F. Simien, M. Remaidi, and C.J. Garrido, Distribution of niobium, tantalum, and other highly incompatible trace elements in the lithospheric mantle: the spinel paradox, *Geochim. Cosmochim. Acta*, **60**, 3, 545–550, 1996.

53. Ionov, D.A., Distribution and residence of lithophile trace elements in minerals of garnet and spinel lherzolites: an ICP-MS study, *J. Conf. Abstr.*, **1**, 1, 278, 1996.

54. Bedini, R.M., J.-L. Bodinier, L., Dautria, and J.-M. Morten, Evolution of LILE-enriched small melt fractions in the lithospheric mantle: a case study from the East African Rift, *Earth Planet Sci. Lett.*, **153**, 67–83, 1997.

55. Dobretsov, N.L., and I.V. Ashchepkov, Melt migration and depletion-regeneration processes in upper mantle of continental and ocean rift zones, in *Ophiolite genesis and evolution of oceanic lithosphere*, eds. T. Peters, A. Nicolas, and R.G. Colman, 125–147, Kluwer Academic Publishers, Dordrecht—Boston—London, 1991.

56. Glaser, S.M., S.F. Foley, and D. Gunter, Trace element enrichment by melt infiltration in garnet- and spinel peridotite xenoliths from the Vitim volcanic field, Transbaikalia, eastern Siberia (The composition, deep structure, and evolution of continents), *Lithos*, **48**, 263–285, 1999.

57. Ashchepkov, I.V., L. André, V.G. Malkovets, Yu.D. Litasov, and A.V. Travin, The stages of the melt percolation in the mantle beneath Vitim (TransBaikal), *J. Conf. Abstr.*, **4**, 1, 362, 1998.

58. Ashchepkov, I.V., V.J.R. Salters, and L. André, Relationships between garnet and clinopyroxene in Vitim

mantle xenoliths: evidence of the polystage growth and melt percolation, *7th Intern. Kimberlite Conf., Extended abstr.*, 35–36, Cape Town, 1998.

59. Sobolev, S.V., and S.G. Siplivets, Evolution of the system 'magmatic chamber-magmatic fissure', *Dokl. AN SSSR*, **297**, 5, 1091–1096, 1986.

60. Ionov, D.A., and E. Jagoutz, Sr and Nd isotopic compositions of minerals from garnet and spinel peridotite xenoliths of the Vitim plateau: first data for mantle xenoliths in the USSR, *Dokl. AN SSSR*, **301**, 5, 232–236, 1988.

61. Evensen, N.M., P.J. Hamilton, and R.K. O'Nion, Rare Earth abundances in chondritic meteorites, *Geochim. Cosmochim. Acta*, **42**, 1199–1212, 1978.

Editorial responsibility: N.L. Dobretsov

Received 20 December 2000
Accepted 16 July 2001